Extending the SBUV PMC Data Record with OMPS NP

Matthew T. DeLand[1] and Gary E. Thomas[2]

[1]Science Systems and Applications, Inc. (SSAI), Lanham, Maryland 20706 USA

[2]Laboratory for Atmospheric and Space Physics (LASP)/University of Colorado, Boulder, Colorado 80303 USA

Correspondence to: Matthew DeLand (matthew.deland@ssaihq.com)

Abstract. We have utilized Solar Backscatter Ultraviolet (SBUV) instrument measurements of atmospheric radiance to create a 40-year record of polar mesospheric cloud (PMC) behavior. While this series of measurements is nearing its end, we show in this paper that Ozone Mapping and Profiling Suite (OMPS) Nadir Profiler (NP) instruments can be added to the merged SBUV PMC data record. Regression analysis of this extended record shows smaller trends in PMC ice water content (IWC) since approximately 1998, consistent with previous work. Current trends are significant at the 95% confidence level in the Northern Hemisphere, but not in the Southern Hemisphere. The PMC IWC response to solar activity has decreased in the Northern Hemisphere since 1998, but has apparently increased in the Southern Hemisphere.

1. Introduction.

Determination of long-term (multi-decadal) variations in the Earth's mesosphere (60-100 km) is challenging. In situ measurements can only be made by rockets that provide a brief snapshot of local conditions. Ground-based measurements of key parameters (e.g. temperature, water vapor, winds) are only available at selected locations. While some data sets are quite long (e.g. phase height (Peters et al. (2017)), other potentially valuable data sets have gaps. Some relevant satellite datasets do exist (e.g. Upper Atmospheric Research Satellite (UARS) Halogen Occultation Experiment (HALOE) (Hervig and Siskind, 2006), Aura Microwave Limb Sounder (MLS) (Lambert et al., 2007; Schwarz et al., 2008), and Thermosphere-Ionosphere-Mesosphere Energetics and Dynamics (TIMED) Sounding of the Atmosphere using Broadband Radiometry (SABER) (Remsberg et al., 2008). However, since the lifetime of a single instrument is

34 generally limited to 10-15 years, maintaining continuity for a specific parameter over multiple

35 decades again becomes an issue.

36

37 Another option is to measure an observable quantity that provides indirect information about the

38 background state of the mesosphere. Polar mesospheric clouds (PMCs) are observed only at

39 high latitudes (typically >50°) and high altitudes (80-85 km) during summer months in each

40 hemisphere. They are formed from small ice crystals (~20-80 nm radius), whose formation and

41 evolution are very sensitive to the temperature (< 150 K) and water vapor abundance near the

42 mesopause. Recent work (e.g. Hervig et al. (2009), Rong et al. (2014), Hervig et al. (2015),

43 Berger and Lübken (2015), Hervig et al. (2016)) has shown quantitative relationships between

44 PMC observables (occurrence frequency, albedo, ice water content) and mesospheric

45 temperature and water vapor.

46

47 The Solar Backscatter Ultraviolet (SBUV) instrument (Heath et al., 1975) was originally

48 launched on the Nimbus-7 satellite in 1978 to measure stratospheric profile and total column

49 ozone, using nadir measurements of backscattered UV radiation between 250-340 nm at

50 moderate spatial resolution (170 km x 170 km footprint). Thomas et al. (1991) showed that these

51 measurements could also be analyzed to identify bright PMCs as an excess radiance signal above

52 the Rayleigh-scattered sky background, modified by ozone absorption. These measurements

53 have been extended by the second generation SBUV/2 instrument, which has been flown

54 successfully on seven NOAA satellites from 1985 to the present. DeLand et al. (2003) describes

55 the extension of the SBUV PMC detection algorithm to SBUV/2 measurements. We use the

56 general term "SBUV" to describe these instruments unless a specific satellite is being discussed.

57 All SBUV instruments have been flown in sun-synchronous orbits, which provide measurements

58 up to ±81° latitude. However, each satellite has drifted from its original Equator-crossing time

59 (typically 1340-1400 LT), so that the local time of measurements at any specific latitude varies

60 over the lifetime of the instrument.

61

62 The consistent design of all SBUV/2 instruments allows the same PMC detection algorithm to be

63 used with each data set, and the overlapping lifetime of these instruments (Figure 1) enables the

64 creation of a merged data set long enough to be used for trend studies. Development and updates

65 to this data set have been published by DeLand et al. (2006), DeLand et al. (2007), Shettle et al.

66 (2009), and DeLand and Thomas (2015). Additional recent studies of long-term PMC behavior

67 that use the SBUV PMC data set include Hervig and Stevens (2014), Berger and Lübken (2015),

68 Hervig et al. (2016), Fiedler et al. (2017), Kuilman et al. (2017), and von Savigny et al. (2017).

69

70
71
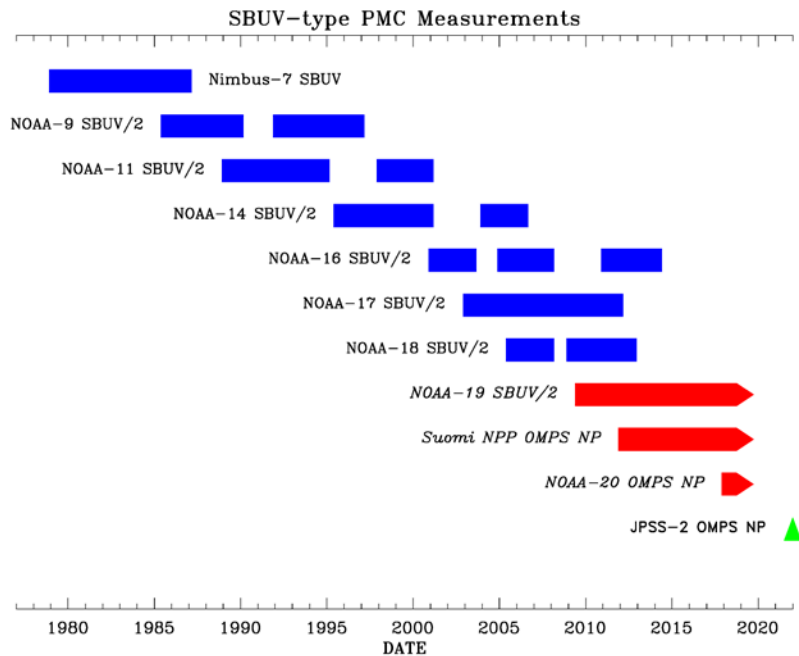
72 **Figure 1.** Timeline of SBUV instrument measurements used for PMC analysis.

73 Blue color indicates inactive instruments. Arrowheads and red color indicate

74 active instruments. Green color indicates planned instrument. Gaps for many

75 SBUV/2 instruments reflect satellite drift into a near-terminator orbit where the

76 current PMC detection algorithm does not function well.

77

78 The last SBUV/2 instrument is now flying on the NOAA-19 spacecraft. Its sun-synchronous

79 orbit has drifted significantly from its original 1340 LT ascending node Equator-crossing time

80 (current Equator-crossing time = 1615 LT), which will interrupt the ability to extract PMC

81 information in 2019 or 2020 due to the decrease in solar zenith angle range available for daytime

82 measurements. Fortunately, the SBUV measurement concept is being continued by the Ozone

83 Mapping and Profiling Suite (OMPS) Nadir Profiler (NP) instrument (Seftor et al., 2014), which

84 is now orbiting on two satellites. This paper will describe updated PMC trends that extend the

3

85   work of DeLand and Thomas (2015), including the addition of OMPS NP data to the 40-year

86   merged SBUV PMC dataset. Section 2 of this paper presents PMC occurrence frequency and ice

87   water content (IWC) results from concurrent measurements by the NOAA-19 SBUV/2 and

88   Suomi National Polar-orbiting Partnership (S-NPP) OMPS NP instruments. We then use these

89   data in Section 3 to extend the long-term IWC trend analysis of DeLand and Thomas (2015) into

90   2018, thus creating a 40-year merged PMC data set. We find that separating this data set into

91   two sections, with a break point selected in 1998 (as described in that section), provides an

92   effective characterization of PMC behavior throughout this long data record.

93

94   **2. OMPS NP Data**

95

96   The OMPS NP instrument was developed to provide ozone data that are consistent with the

97   SBUV/2 series of instruments (Flynn et al., 2014). The first OMPS NP instrument was launched

98   on the Suomi National Polar-orbiting Partnership (S-NPP) satellite on 28 October 2011, and

99   began collecting regular data in January 2012. It makes hyperspectral measurements covering

100   the 250-310 nm spectral region, with a sampling of approximately 0.6 nm. We utilize radiance

101   measurements interpolated to the five shortest SBUV/2 wavelengths (nominally 252.0, 273.5,

102   283.1, 287.6, 292.3 nm) to provide continuity with the current SBUV PMC detection algorithm.

103   Potential retrieval improvements based on a different wavelength selection will be explored in

104   the future. The NP instrument uses a larger field of view (250 km x 250 km at the surface)

105   compared to a SBUV/2 instrument. We will show that this difference does not affect the ability

106   of the NP instrument to track seasonal PMC behavior.

107

108   The only revision implemented to the SBUV PMC detection algorithm for OMPS NP is to derive

109   a solar zenith angle-dependent detection threshold in albedo that is based on NP end-of-season

110   measurements, rather than SBUV measurements. This update ensures that any change in

111   background variability introduced by the larger NP field of view is addressed. Figure 2 shows

112   the NP threshold function derived as a quadratic fit to data taken during 11-31 August 2012,

113   when very few PMCs are typically detected in SBUV-type data. Note that for a nadir-viewing

114   instrument such as NP, the solar zenith angle (SZA) is equivalent to the supplement of the

115   scattering angle (SCA), i.e. SZA = 180° - SCA. The SBUV/2 threshold function determined by

116   DeLand and Thomas (2015) is shown for comparison, where an empirical scaling factor of 1.6 is

117   also applied to eliminate "false positive" PMC detections at the start and end of the PMC season.

118   These functions differ slightly at low solar zenith angle, but are almost identical at SZA > 50°.

119   The uncertainty in this detection threshold is approximately $\pm 3 \times 10^{-6}$ sr^{-1}. This value is driven by

120   albedo fluctuations due to meridional variations in stratospheric ozone, since the magnitude of

121   the backscattered albedo at wavelengths used for PMC detection (250-290 nm) is dominated by

122   ozone absorption.

123

124   DeLand and Thomas (2015) noted that fluctuations in 252 nm albedo (caused by lower signal-to-

125   noise performance relative to other wavelengths) could lead to unrealistically faint scenes being

126   identified as PMC detections. They implemented an additional requirement for trend analysis

127   that the albedo residual at 273 nm be greater than 3×10^{-6} sr^{-1} at all SZA. Converting this albedo

128   value into IWC gives an effective threshold that ranges between 35-40 g km^{-2}, as shown in

129   Figure 2. This value is consistent with the IWC threshold of 40 g km^{-2} determined by Hervig

130   and Stevens (2014) for their analysis of SBUV PMC data. It is important to note that additional

131   tests focusing on spectral dependence of the albedo residuals are also applied to positively

132   identify any sample as a PMC.

133
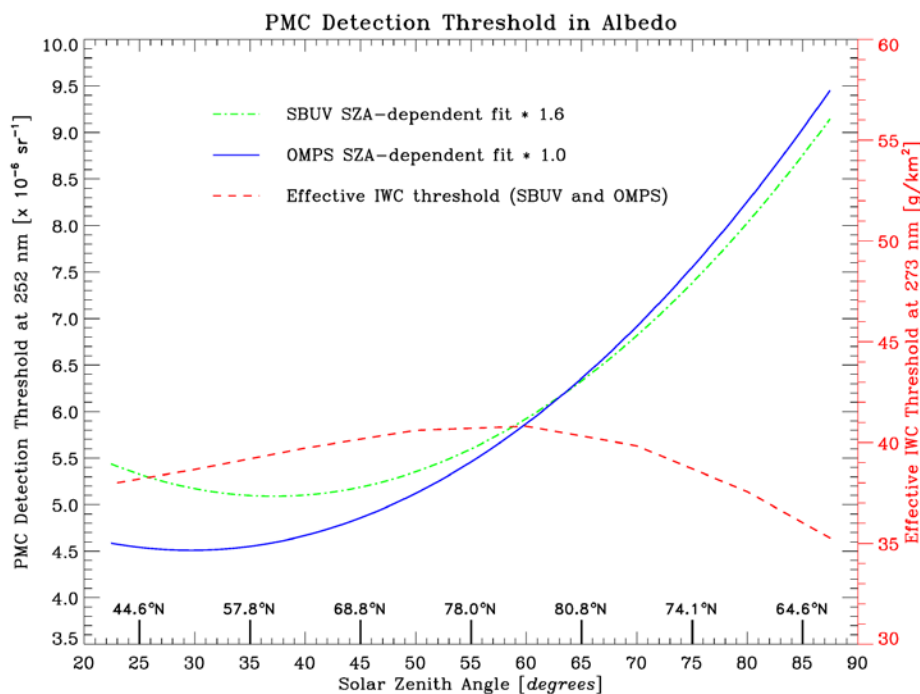
134

135

136   **Figure 2.** PMC detection threshold functions plotted *vs.* solar zenith angle

137   (SZA). The quadratic fit in SZA used by DeLand and Thomas (2015) for

138   SBUV/2 processing, derived from NOAA-18 data taken in 2007 days 222-242, is

139   shown as the dot-dash line (green). The quadratic fit in SZA used for OMPS NP

140   data in this paper, derived from S-NPP data taken in 2012 days 222-242, is shown

141   as the solid line (red). The local time sampling is very similar (1335 LT Equator-

142   crossing time for NOAA-18, 1340 LT Equator-crossing time for S-NPP). The

143   effective IWC threshold (described in the text) is shown as the dashed line (red),

144   and referenced to the scale on the right-hand Y-axis. Nominal latitude values for

145   June 21 are identified on the bottom of the plot.

146

147   Figure 3 illustrates the PMC detection results obtained for a single day of S-NPP OMPS NP data.

148   The top panel shows the individual albedo values at 273.7 nm for all 14 orbits. These values are

149   tightly grouped in SZA because OMPS NP uses a measurement sequence that begins at the

150   Southern Hemisphere terminator (SZA $= 90°$) for each orbit, and continues in 38 second

151   increments throughout the day side of the orbit. There is very little change in latitude for the

152   terminator crossing during a single day, which leads to repeatable sample latitudes on the same

153   time scale, although the terminator crossing location does shift over the course of the PMC

154   season. Samples identified as PMCs are shown as squares. The bottom panel shows the albedo

155   residual (difference between observation and background fit) for the same date. Note that an

156   arbitrary PMC would be expected to have a stronger signal in albedo at lower scattering angles

157   (= higher SZA) due to the forward scattering peak of the small ice particles (DeLand et al., 2011;

158   Lumpe et al., 2013). We do not adjust the observed albedo values with any assumed phase

159   function before applying our PMC detection algorithm, so the SZA dependence of the albedo

160   threshold shown in Figure 2 represents a method to incorporate this sensitivity in our analysis.

161   The spread of the non-PMC albedo residual values due to both longitudinal and along-track

162   ozone variability is $\sim 3\text{-}5\times10^{-6}$ sr^{-1} at latitudes less than approximately $60°$ (SZA $< 40°$), and

163   increases slightly at higher latitudes where ozone variability is greater.

164

165 Some improvement in the detection of faint PMCs using this algorithm is possible when

166 measurements are spaced closely enough in time that the background fit can be calculated

167 separately for each orbit, thus eliminating the effects of longitudinal variations in ozone.

168 DeLand et al. (2010) used this approach with Aura OMI data, which have a 13 km along-track

169 sampling. Even with these data, though, non-PMC samples at low latitude still fluctuate by

170 $\pm 3 \times 10^{-6}$ sr^{-1} around the background fit (see their Figure 5). The minimum PMC detection

171 threshold for nadir-only measurements is thus higher than the level available to an instrument

172 such as CIPS that incorporates multiple viewing angles, and the accompanying phase function

173 information, to separate clouds from background samples.

174
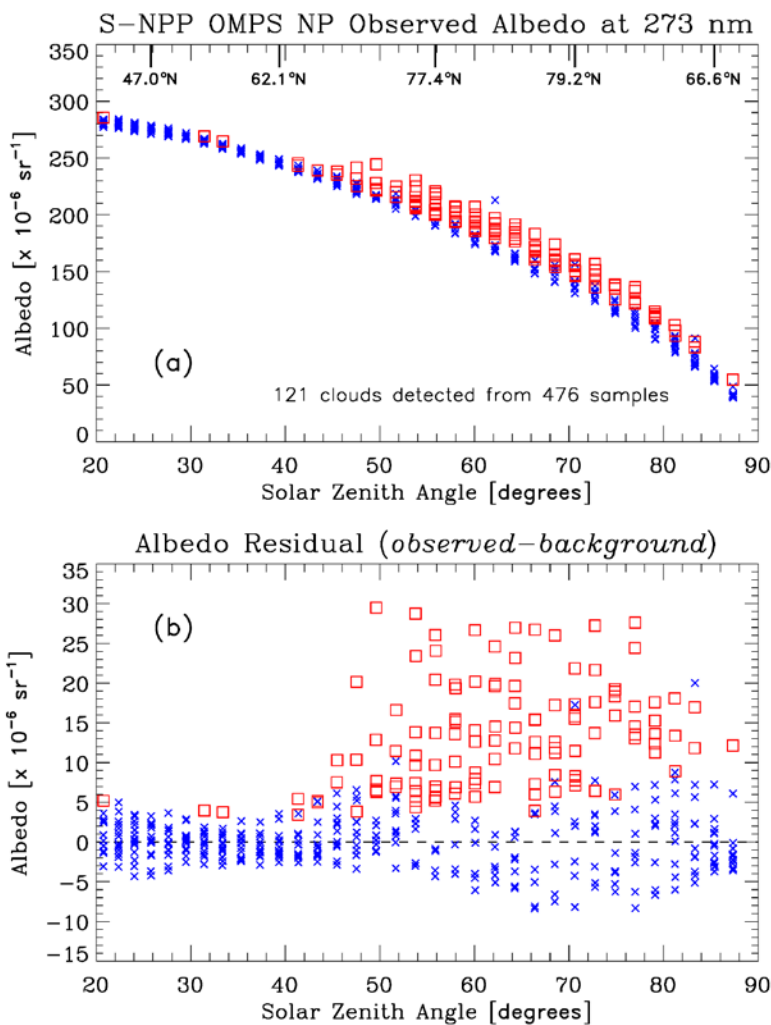
175

176

177   **Figure 3.** (a) S-NPP OMPS NP 273 nm albedo values for all measurements on
178   2018 day 189. Squares (red) indicate measurements identified as PMCs by the
179   detection algorithm. Crosses (blue) indicate non-PMC samples. Tick marks (top
180   X-axis) show approximate latitudes corresponding to selected solar zenith angle
181   values. (b) 273 nm albedo residuals (observed-background fit) for the
182   measurements shown in panel (a). PMC detections are indicated by squares.

183

184   The fluctuations in the background data represent a significant component of the uncertainty in

185   PMC albedo for any individual detection. Using the uncertainty analysis described in DeLand et

186   al. (2003), we estimate that this term gives a value of ~2×10^{-6} sr^{-1} for PMC albedo uncertainty at

187   273 nm for most latitudes. There is also a possible bias in PMC albedo due to the presence of

188   faint (but otherwise valid) clouds in the background fit calculation. Examination of the seasonal

189   variation in background fit at fixed SZA values suggests that there is no bias at latitudes less than

190   ~70°, increasing to a possible bias of ~$2\text{-}3\times10^{-6}$ sr^{-1} at 75°-81° latitude.

191

192   We next compare S-NPP OMPS NP PMC occurrence frequency and ice water content (IWC)

193   seasonal average results to concurrent NOAA-19 SBUV/2 PMC results for seven Northern

194   Hemisphere (NH) and six Southern Hemisphere (SH) PMC seasons from NH 2012 through NH

195   2018. IWC values are derived from PMC albedo values using the albedo-ice regression (AIR)

196   approach described in DeLand and Thomas (2015). This approach parameterizes output from a

197   coupled general circulation model and microphysical model to create linear fits for IWC as a

198   function of PMC albedo at multiple scattering angles. Thomas et al. (2018) present a more

199   extensive description of the AIR approach. Figures 4-6 show these comparisons for the latitude

200   bands 50°-64°, 64°-74°, and 74°-82° respectively. We define the length of each season as [-20

201   days since solstice (DSS), +55 DSS] for PMC trend analysis, following the discussion presented

202   in DeLand and Thomas (2015). All averages use both ascending node and descending node data

203   where available. Since most of the uncertainty in IWC values comes from random variations in

204   albedo, as discussed in DeLand et al. (2007), we show the standard error [(standard deviation) /

205   (number of clouds)$^{1/2}$] of each seasonal average IWC value in the right-hand panels. The

206   nominal SZA and local time values for these averages are given in Table 1, as well as the total

207   number of samples and PMCs detected. The two instruments agree very well in both absolute

8

208 level and interannual variability for both quantities in each latitude band. The occurrence

209 frequency difference between instruments in the NH 2016 season at 64°-74° N (Figure 5(a)) is

210 anomalous, and does not appear in IWC results for the same season (Figure 5(b)). We believe

211 that the S-NPP OMPS result is the outlier in this case. We are satisfied that S-NPP OMPS NP

212 data can be added to the SBUV PMC data set to continue the long-term record in a consistent

213 manner.

214
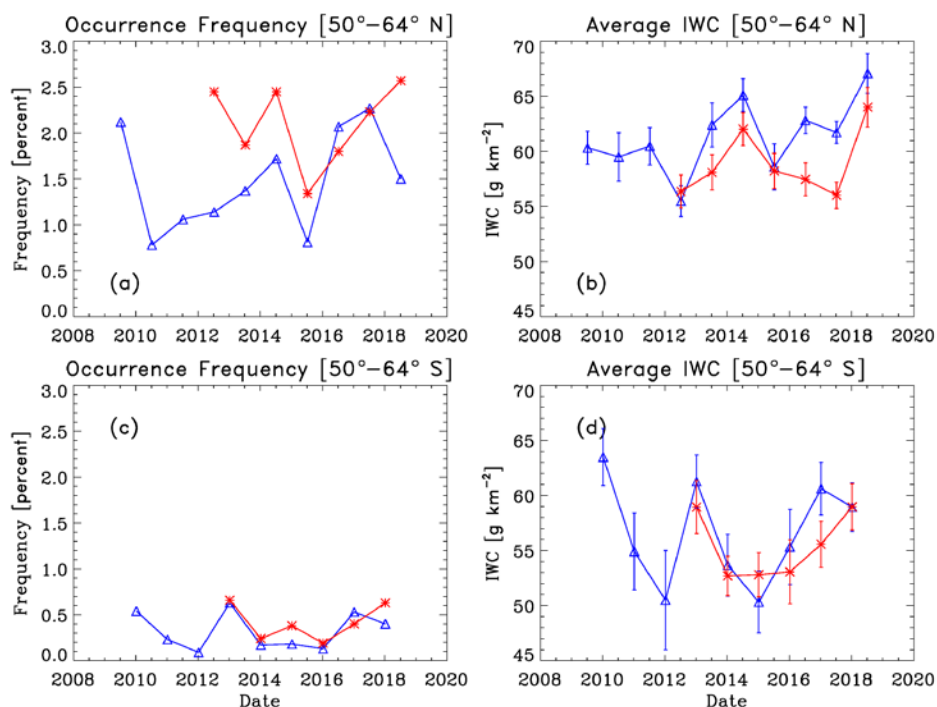
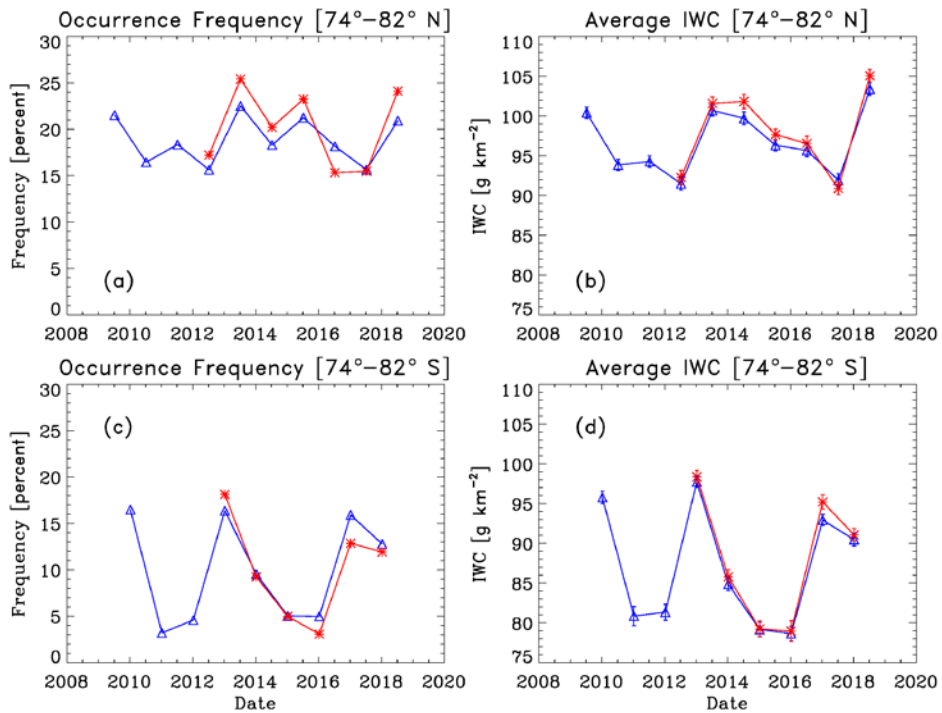217 **Figure 4.** Season average PMC occurrence frequency and ice water content data

218 at 50°-64° latitude. Blue = NOAA-19 SBUV/2, red = S-NPP OMPS. Left side =

219 occurrence frequency [percent], right side = IWC [g km^{-2}]. Top row = Northern

220 Hemisphere, bottom row = Southern Hemisphere. Average SZA and local time

221 values for each instrument during each season are listed in Table 1.

222

223

224
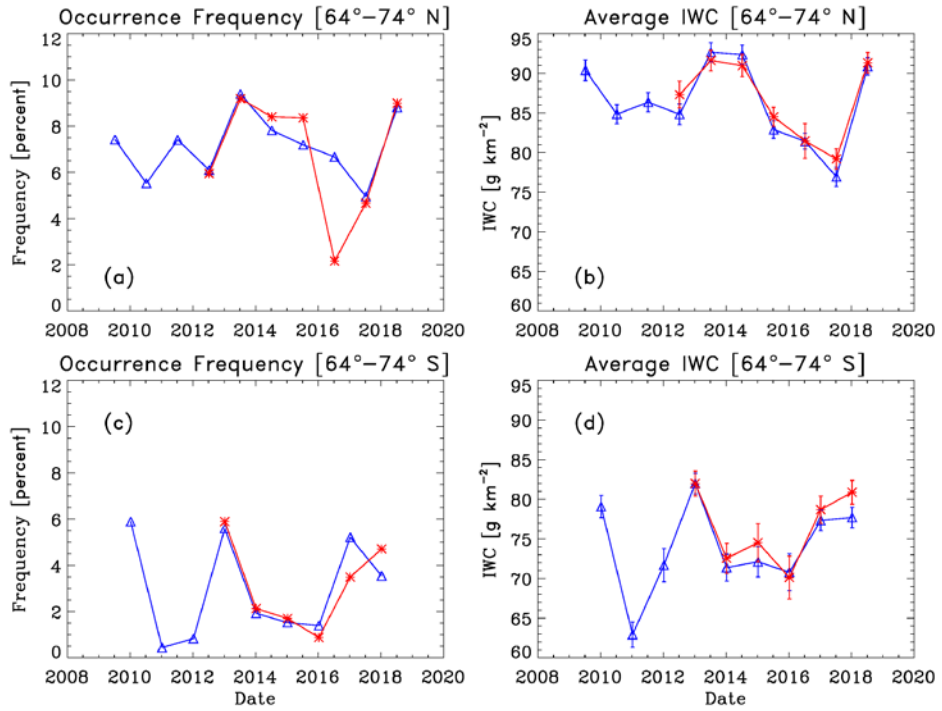
225   **Figure 5.** Season average occurrence frequency and IWC data at 64°-74°

226   latitude. Identifications are as in Figure 4.

227

228

229

230   **Figure 6.** Season average occurrence frequency and IWC data at 74°-82°

231   latitude. Identifications are as in Figure 4.

232

233   Some model results (e.g. Stevens et al. (2017) show significantly higher PMC occurrence

234   frequency values (factor of 5-10) for clouds that exceed the nominal SBUV IWC threshold of 40

235   g km^{-2}. However, there are important factors that should also be considered in such

236   comparisons. The use of an idealized PMC formation mechanism based on bulk thermodynamic

237   properties (Hervig et al., 2009) in the model calculations will yield a high amount of PMCs in

238   many situations. Using only results from the peak of the diurnal cycle at 4 LT, as chosen by

239   Stevens et al. (2017), will produce substantially higher frequency values than those determined

240   in this paper by averaging both ascending node (10-13 LT) and descending node (3-5 LT) data.

241   Stevens et al. (2017) calculate seasonal averages using only the core of the NH season in July

242   (DSS = [+10,+40]), which can give a factor of two or more higher occurrence frequency values

243   compared to the longer season definition used in this paper. Fiedler et al. (2017) show seasonal

244   average occurrence frequency values between 3-12% during 1997-2015 for strong clouds (most

245   similar to SBUV detections) observed by the Arctic Lidar Observatory for Middle Atmosphere

246   Research (ALOMAR) lidar at 69°N, which is similar to the SBUV/2 and OMPS frequency

247   values shown in Figure 5(b) for 64°-74°N. Schmidt et al. (2018) show seasonal occurrence

248   frequency values from the Mesospheric Ice Microphysics And tranSport (MIMAS) model at

249   69°N that are consistent with ALOMAR results for strong clouds.

250

251   Hervig and Stevens (2014) suggest that there may be a bias in the SBUV background calculation,

252   based on their analysis of the number of selected (as PMC) and non-selected SBUV samples

253   above a constant albedo threshold (5x10^{-6} sr^{-1} at 252 nm). This approach is not correct at low

254   scattering angle (high SZA), since our actual threshold for the V3 product that they consider is

255   determined by the SZA-dependent function shown in Figure 2. We have examined the seasonal

256   variation of our background fit at fixed SZA values. We find no evidence for background error

257   at 65°-70° latitude, but a possible high bias during the core of the PMC season of ~2-3x10^{-6} sr^{-1}

258   at 75°-81° latitude. It is difficult to determine whether this result represents faint PMCs that are

259   "embedded" in the background data and not currently identified (thus representing a bias), or

260   whether it indicates increased stratospheric ozone variability for this latitude and time of year.

261

262   The nadir viewing geometry of SBUV and OMPS means that only bright PMCs, composed of

263   relatively large ice particles, will be detected above the Rayleigh scattering background. Our

264   SBUV PMC detection algorithm does not yield particle size, but estimates can be made based on

265   other methods. Bailey et al. (2015) state that CIPS detects almost 100% of PMCs with a mean

266   particle radius greater than 30 nm, based on a nominal brightness of 2×10^{-6} sr^{-1} and a 90°

267   scattering angle. Lumpe et al. (2013) quote a CIPS detection threshold of IWC > 10 g km^{-2}. The

268   minimum SBUV IWC value is ~40 g km^{-2} based on our albedo threshold (Figure 2), which is

269   consistent with the empirical result derived by Hervig and Stevens (2014). They find a median

270   particle size of $r_m \approx 30$ nm for their long-term analysis of the SBUV record, using only data

271   measured between 9-15 LT, compared to a median size of $r_m \approx 38$ nm for SBUV measurements

272   used in SOFIE-SBUV coincidence studies. In addition, SBUV PMCs are only observed at

273   scattering angles greater than 90°, which will give a lower PMC brightness for a given particle

274   size compared to the CIPS definition. These factors suggest that SBUV and OMPS instruments

275   only detect PMCs with mean particle radius > 35-40 nm. Stevens et al. (2017) calculated daily

276   average IWC during July 2009 as a function of latitude, using output from the NOGAPS-

277   ALPHA forecast-assimilation system and the Hervig et al. (2009) 0-D model to create IWC

278   values from these data. When they apply a threshold of IWC > 40 g km^{-2}, their zonal average

279   results are approximately 20-30% greater than the NOAA-19 SBUV/2 seasonal average values

280   for NH 2009 shown in Figure 4(b), Figure 5(b), and Figure 6(b). Possible causes for this

281   difference include the use of July-only averages compared to the longer season defined in this

282   paper, the averaging of model results at all local times compared to the specific local time of the

283   measurements (plus local time adjustment described in Section 3), and the different methods

284   used to create IWC values.

285

286   **3. Trend Update**

287

288   Our analysis of long-term trends in SBUV PMC data follows the approach presented in DeLand

289   et al. (2007), and updated by DeLand and Thomas (2015). We use IWC as our key variable for

290   trend analysis because it provides a way of minimizing the effects due to variations in scattering

291   angle caused by the drifting orbit of many SBUV instruments. The seasonal average IWC values

292   do not incorporate frequency variation, i.e. only samples with a positive PMC detection are used.

293   This choice reduces the magnitude of interannual fluctuations, particularly in the SH where

294   SBUV occurrence frequency results are more variable, and allows us to focus on a quantity

295   [IWC derived from measured albedo] that we feel most confident in evaluating. Long-term

296   trends in SBUV PMC frequency were derived by Shettle et al. (2009), and are also considered in

297   Pertsev et al. (2014). As in our earlier publications, we use a multiple regression fit of the form

298

299          $X_{fit}(latitude, t) = A(latitude)*F_{Ly\alpha}(t) + B(latitude)*(t-1979) + C(latitude)$ [1]

300

301   where $F_{Ly\alpha}(t)$ is the composite solar Lyman alpha flux dataset available from the LASP

302   Interactive Solar Irradiance Data Center (LISIRD) and averaged over the appropriate NH or SH

303   season. We assess the quantitative significance of the trend term by calculating a 95%

304   confidence limit as described in DeLand et al. (2007), using a method presented by Weatherhead

305   et al. (1998) that accounts for periodicity auto-correlation in addition to the fit uncertainty.

306

307   The orbit drift experienced by most SBUV instruments causes significant changes in local time

308   sampling for any selected latitude band over our 40-year PMC data record. Since lidar

309   measurements show significant local time dependence in PMC properties (e.g. Chu et al., 2006;

310   Fiedler et al., 2011), it must be addressed for trend analysis. One approach is to define a limited

311   local time range that is always sampled (Hervig and Stevens, 2014; Hervig et al., 2016).

312   However, this reduces the amount of data available (only ascending or descending node data can

313   be used except near 81° latitude), and the time range must be adjusted for different latitude

314   bands. We have chosen to apply a diurnal harmonic function to normalize all observations to a

315   single local time (11 hr LT). The derivation of this function from SBUV data is described in

316   detail by DeLand and Thomas (2015).

317

318            $F(t) = A_0 + A_{24}*\cos[(2\pi/24)*(t-\varphi_{24})]$ [1]

319

320        $A_0 = 110$ $A_{24} = 8$ $\varphi_{24} = 2$ hr $F_{norm}(t) = F(t)/F(11\ h)$

321

322   The SBUV local time dependence created by DeLand and Thomas (2015) and used in this paper

323   was based on observations at a limited set of local times. A single diurnal function with a

324   maximum/minimum ratio of ~1.15 was derived for use at all latitudes. This function was shown

325   to have a similar shape, but somewhat smaller amplitude, than lidar-based functions determined

326   by Fiedler et al. (2011) and Chu et al. (2006). Recent model results provide local time

327   dependence functions at different latitude bands for multiple levels of IWC threshold. Stevens et

328   al. (2017) determined a maximum/minimum ratio of ~1.4 for the IWC variation (no frequency

329   weighting) at 90°N in July 2009, using only model PMCs with IWC > 40 g km^{-2}. This ratio

330   decreases slightly at lower latitudes (55°N, 60°N) and higher latitude (80°N). Schmidt et al.

331   (2018) created IWC local time variations from 35 years of model output (1979-2013) for the

332   three broad latitude bands used in this paper (50°-64°N, 64°-74°N, 74°-82°N) and three

333   threshold levels (IWC > 0, > 10, > 40 g km^{-2}). The "strong" cloud results (IWC > 40) all show

334   greater maximum/minimum ratios than the SBUV function, with values increasing from 1.3 at

335   50°-64°N to 2.1 at 74°-82°N. This latitude dependence differs from Stevens et al. (2017) and the

336   Aura OMI results shown by DeLand et al. (2011), where the local time amplitude decreases at

337   higher latitude. We have not yet investigated the impact of using one of these model-based local

338   time dependence functions in our trend analysis.

339

340   We define the duration of the PMC season for our trend analysis as DSS = [-20,+55] to fully

341   capture interannual variations (DeLand and Thomas, 2015). We have also examined the impact

342   of limiting our season to a "core" range of DSS = [+10,+40] to correspond to July in NH summer

343   and January in SH summer, as used in other studies. The numerical values calculated for the

344   trend term do change slightly for each latitude band, as expected. However, the determination of

345   whether a trend result exceeds the 95% confidence level defined above does not change for any

346   latitude band with the use of core seasons. This implies that our conclusions regarding long-term

347   behavior are robust.

348

349   We created a merged SBUV PMC IWC data set for each season and latitude band, using an

350   adaptation of the "backbone" method of Christy and Norris (2004) as discussed by DeLand et al.

351   (2007). An advantage of this method is that it easily accommodates the addition of new

352   instruments such as S-NPP OMPS NP to the overall PMC data set. Normalization adjustment

353   values for each SBUV and OMPS instrument derived from a fit at 50°-82° latitude are applied

354   consistently at all latitude bands. The adjustment values for merging derived in this work are

355   slightly different than those derived by DeLand and Thomas (2015) because the composition of

356   the overall data set has changed, even though the original V4 PMC data sets for each instrument

357   as described in that paper have not changed. Almost all adjustment values are still less than 3%

358   of the seasonal average IWC (e.g. 0.97-1.03), and most of the changes in the adjustment values

359   determined for this paper relative to DeLand and Thomas (2015) are smaller than ±0.01.

360   Performing the trend analysis with no merging adjustments does not change the results for

361   exceeding the 95% confidence level in any latitude band, similar to the core season analysis

362   described above. We have not evaluated this data set for the possibility of longitudinally

363   dependent trends, as was done by Fiedler et al. (2017).

364

365   Berger and Lübken (2011) calculated long-term trends in PMC scattered brightness by coupling

366   3-D atmospheric model runs (driven by lower atmosphere reanalysis data) with a microphysics

367   module that simulates PMC ice particle formation. They found that the long-term trend in

368   mesospheric temperature at 83 km changed from negative to positive in the late 1990s, and

369   suggested that this change was forced by an increase in stratospheric ozone and its subsequent

370   impact on middle atmospheric heating rates. This implies that a single linear segment is not the

371   best way to represent trends since 1978. Since PMC properties are expected to be very

372   responsive to mesospheric temperature changes, DeLand and Thomas (2015) followed this

373   guidance and calculated their PMC trends in two segments, with a break point in 1998. We

374   follow the same approach here and calculate multiple regression fits for two time segments,

375   covering 1979-1997 and 1998-2018 respectively.

376
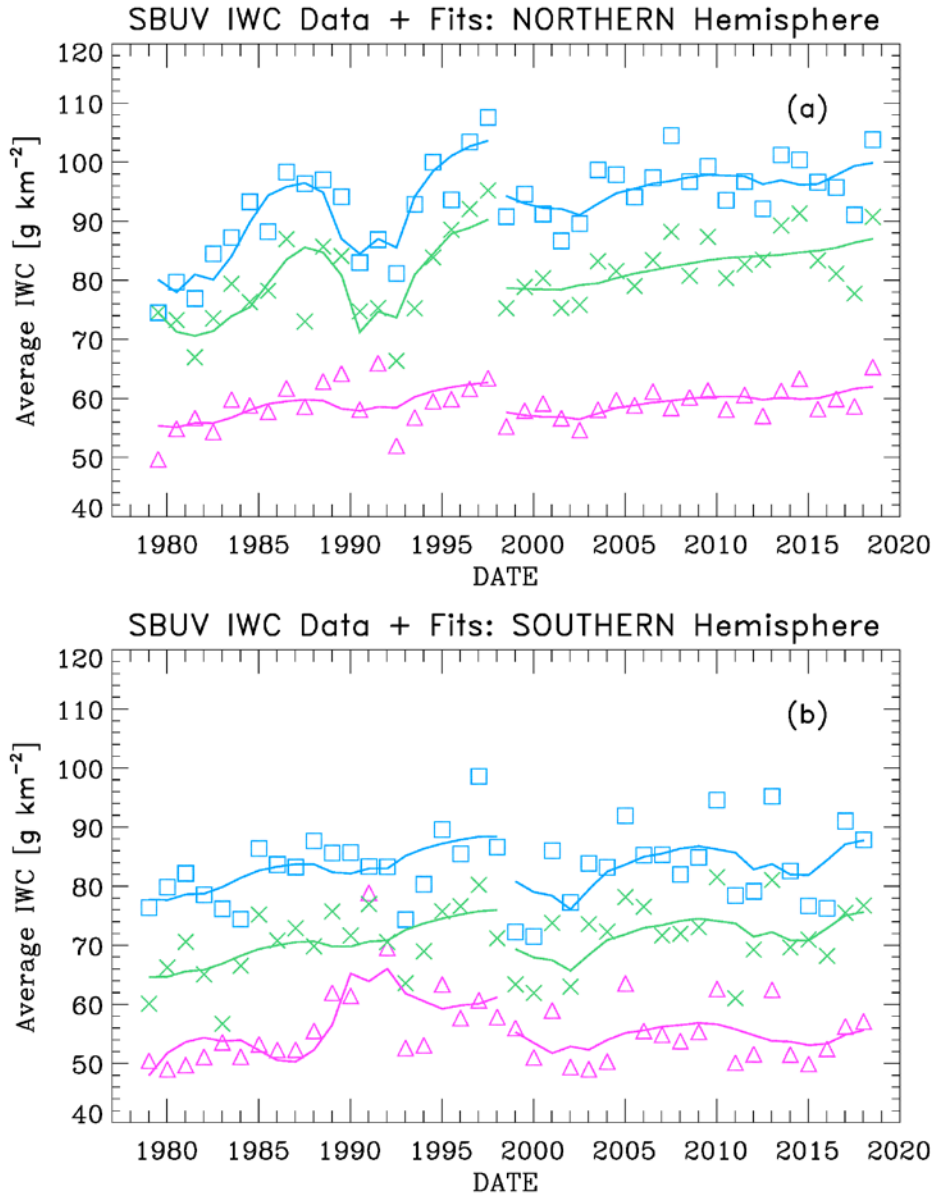
Figure 7. (a) SBUV merged seasonal average IWC values for three different latitude bands: 50°-64° N (purple triangles), 64°-74° N (green crosses), 74°-82° N (blue squares). The solid lines show multiple regression fits to the data for the periods 1979-1997 and 1998-2018. (b) SBUV merged seasonal average IWC values for 50°-64° S, 64°-74° S, and 74°-82° S. The solid lines show fits for the periods 1979-1997 and 1998-2018.

386   The results of these fits are shown in Figure 7, and presented numerically in Tables 2 and 3.

387   Note that a negative sign for the solar activity term implies an anti-correlation, i.e. an increase in

388   solar activity corresponds to a decrease in IWC. This behavior has been explained by variations

389   in solar ultraviolet irradiance, which causes higher temperatures and lower water vapor

390   abundance during solar maximum periods (Garcia, 1989). The trend term and solar term results

391   for each hemisphere are discussed below.

392   a. NH trend term. These results are significant at the 95% confidence level (as defined in

393   the previous paragraph) for all latitude bands in both segments, although the trend values for

394   segment 2 (1998-2018) are smaller than those derived by DeLand and Thomas for a shorter

395   period (1998-2013). The changes in this term do not exceed the $\pm 1\,\sigma$ uncertainty of the current

396   fit results in any latitude band, as shown in Table 2(b).

397   b. SH trend term. These values exceed our 95% confidence limit in segment 1, consistent

398   with DeLand and Thomas (2015). However, the segment 2 trend values are a factor of 2-4

399   smaller than those derived by DeLand and Thomas (2015), and no latitude band reaches the 95%

400   confidence limit. We discuss this result further in part (d). Note that the difference between

401   hemispheres has been explained by Siskind et al. (2005) to be caused by higher SH mesospheric

402   temperatures, making SH PMCs more sensitive to small temperature changes.

403   c. NH solar term. These values are significant at the 95% level for most latitude bands

404   for segment 1, consistent with DeLand and Thomas (2015). Phase lag values of 0.5-1.0 years are

405   found, consistent with previous analysis of SBUV PMC data. The fit values for segment 2 are

406   smaller than those derived for segment 1 by as much as a factor of seven, depending on latitude

407   band, and in general are not larger than the $\pm 1\,\sigma$ uncertainty. This lack of response to solar

408   activity in recent years has also been identified in ALOMAR lidar PMC data (Fiedler et al.,

409   2017) and AIM CIPS data (Siskind et al., 2013).

410   d. SH solar term. These values poleward of 64° latitude are smaller than the $\pm 1\,\sigma$

411   uncertainty in segment 1, but become 2-3 times larger and exceed the 95% significance level in

412   segment 2. However, note also that the correlation coefficient for this term is quite low ($r =$

413   0.19). We speculate that during segment 2, the multiple regression fit algorithm is assigning

414   some of the greater interannual variability in SH data to the solar activity term. The large

415   positive solar term at 50°-64° S is driven by higher IWC values in the 1990-1991 and 1991-1992

416   seasons. In this latitude band, only 10-20 clouds are detected from 6000-8000 samples during

417   the entire season in some years, as shown in Table 1. Fluctuations in only a few samples can

418   thus have a significant impact in such seasons.

419

420   These result illustrate the need for caution in interpreting the results of using a periodic term

421   based on solar variability in a regression fit that covers less than two full solar cycles for a single

422   segment, since variations in a small number of data points near the end of the period can have a

423   substantial impact. However, the large IWC values observed in the recent NH 2018 PMC season

424   did not significantly change the NH solar activity term for this segment. Both the source of the

425   hemispheric difference in solar activity response and the source of the derived phase lag in the

426   NH are not understood.

427

428   **4. Conclusion**

429

430   We have shown that OMPS NP measurements can be used successfully to continue the long

431   PMC data record created from SBUV and SBUV/2 instruments. When we use S-NPP data to

432   extend our merged PMC data set through the NH 2018 season, we find smaller trends in IWC in

433   both hemispheres since 1998 compared to the results shown by DeLand and Thomas (2015).

434   The NH trends continue to be significant at the 95% confidence level, while the SH trends are

435   now slightly smaller than this threshold. The calculated sensitivity to solar activity during 1998-

436   2018 is a factor of three to six smaller than the 1979-1997 result for NH data poleward of 64° N.

437   However, the solar activity sensitivity for SH data increases by a factor of three to four for the

438   1998-2018 period, and becomes statistically significant at all latitudes. We will continue to

439   investigate possible causes for this change in behavior and hemispheric discrepancy.

440

441   A second OMPS NP instrument was launched on the NOAA-20 (formerly JPSS-1) satellite in

442   November 2017, and is now collecting regular data. Three more OMPS NP instruments are

443   scheduled for launch on JPSS satellites at regular intervals through approximately 2030. All of

444   the satellites carrying OMPS NP instruments will be kept in an afternoon equator-crossing time

445   sun-synchronous orbit, so that orbit drift (which has impacted all SBUV/2 instruments) will not

446   affect the ability to retrieve PMC information. We therefore anticipate extending the continuous

447   SBUV PMC data record to 60 years to support long-term climate studies.

449
450
451

453
454
455

457
458
459
460
461
462
463
464

References

Bailey, S. M., Thomas, G. E., Hervig, M. E., Lumpe, J. D., Randall, C. E., Carstens, J. N., Thurairajah, B., Rusch, D. W., Russell III, J. M., and Gordley, L. L.: Comparing nadir and limb observations of polar mesospheric clouds: The effect of the assumed particle size distribution, J. Atmo. Solar-Terr. Phys., 127, 51-65, doi:10.1016/j.jastp.2015.02.007, 2015.

Berger, U., and Lübken, F.-J.: Mesospheric temperature trends at mid-latitudes in summer, Geophys. Res. Lett., 38, L22804, doi:10.1029/2011GL049528, 2011.

Berger, U., and Lübken, F.-J.: Trends in mesospheric ice layers in the Northern Hemisphere during 1961-2013, J. Geophys. Res. Atmos., 120, doi:10.1002/2015JD023355, 2015.

Chu, X., Espy, P. J., Nott, G. J., Diettrich, J. C., and Gardner, C. S.: Polar mesospheric clouds observed by an iron Boltzmann lidar at Rothera (67.5S, 68.0W), Antarctica from 2002 to 2005: Properties and implications, J. Geophys. Res. Atmos., 111, D20213, doi:10.1029/2006JD007086, 2006.

Christy, J. R., and Norris, W. B.: What may we conclude about global temperature trends?, Geophys. Res. Lett., 31, L06211, doi:10.1029/2003GL019361, 2004.

DeLand, M. T., and Thomas, G. E.: Updated PMC trends derived from SBUV data, J. Geophys. Res. Atmos., 120, doi:10.1002/2014JD022253, 2015.

DeLand, M. T., Shettle, E. P., Thomas, G. E., and Olivero, J. J.: Solar backscattered ultraviolet (SBUV) observations of polar mesospheric clouds (PMCs) over two solar cycles, J. Geophys. Res., 108(D8), 8445, doi:10.1029/2002JD002398, 2003.

DeLand, M. T., Shettle, E. P., Thomas, G. E., and Olivero, J. J.: A quarter-century of satellite PMC observations, J. Atmos. Solar-Terr. Phys., 68, 9-29, 2006.

DeLand, M. T., Shettle, E. P., Thomas, G. E., and Olivero, J. J.: Latitude-dependent long-term variations in polar mesospheric clouds from SBUV Version 3 PMC data, J. Geophys. Res., 112, D10315, doi:10.1029/2006JD007857, 2007.

DeLand, M. T., Shettle, E. P., Levelt, P. F., and Kowalewski, M.: Polar mesospheric clouds (PMCs) observed by the Ozone Monitoring Instrument (OMI) on Aura, J. Geophys. Res., 115, D21301, doi:10.1029/2009JD013685, 2010.

DeLand, M. T., Shettle, E. P., Thomas, G. E., and Olivero, J. J.: Direct observations of PMC local time variations by Aura OMI, J. Atmos. Solar-Terr. Phys., 73, 2049-2064, doi:10.1016/j.jastp.2010.11.019, 2011

Fiedler, J., Baumgarten, G., Berger, U., Hoffman, P., Kaifler, N., and Lübken, F.-J.: NLC and the background atmosphere above ALOMAR, Atmos. Chem. Phys., 11, 5701-5717, doi:10.5194/acp-11-5701-2011, 2011.

Fiedler, J., Baumgarten, G., Berger, U., and Lübken, F.-J.: Long-term variations of noctilucent clouds at ALOMAR, J. Atmos. Solar-Terr. Phys., 162, 79-89, doi:10.1016/j.jastp.2016.08.006, 2017.

Flynn, L., Long, C., Wu, X., Evans, R., Beck, C. T., Petropavlovskikh, I., McConville, G., Yu, W., Zhang, Z., Niu, J., Beach, E., Hao, Y., Pan, C., Sen, B., Novicki, M., Zhou, S., and Seftor, C.: Performance of the Ozone Mapping and Profiling Suite products, J. Geophys. Res. Atmos., 119, 6181-6195, doi:10.1002/2013JD020467, 2014.

Garcia, R. R.: Dynamics, radiation, and photochemistry in the mesosphere: Implications for the formation of noctilucent clouds, J. Geophys. Res., 94, 14605-14615, 1989.

Heath, D. F., Krueger, A. J., Roeder, H. A., and Henderson, B. D.: The Solar Backscatter Ultraviolet and Total Ozone Mapping Spectrometer (SBUV/TOMS) for Nimbus G, Opt. Eng., 14, 323-331, 1975.

Hervig, M., and Siskind, D.: Decadal and inter-hemispheric variability in polar mesospheric clouds, water vapor, and temperature, J. Atmos. Solar Terr. Phys., 68, 30-41, doi:10.1016/j.jastp.2005.08.010, 2006.

Hervig, M. E., and Stevens, M. H.: Interpreting the 35-year SBUV PMC record with SOFIE observations, J. Geophys. Res. Atmos., 119, doi:10.1002/2014JD021923, 2014.

Hervig, M. E., Stevens, M. H., Gordley, L. L., Deaver, L. E., Russell III, J. M., and Bailey, S. M.: Relationships between polar mesospheric clouds, temperature, and water vapor from Solar Occultation for Ice Experiment (SOFIE) observations, J. Geophys. Res., 114, D20203, doi:10.1029/2009JD012302, 2009.

Hervig, M. E., Siskind, D. E., Bailey, S. M., and Russell III, J. M.: The influence of PMCs on water vapor and drivers behind PMC variability from SOFIE observations, J. Atmos. Solar Terr. Phys., 132, 124-134, doi:10.1016/j.jastp.2015.07.010, 2015.

Hervig, M. E., Berger, U., and Siskind, D. E.: Decadal variability in PMCs and implications for changing temperature and water vapor in the upper mesosphere, J. Geophys. Res. Atmos., 121, 2383-2392, doi:10.1002/2015JD024439, 2016.

Kuilman, M., Karlsson, B., Benze, S., and Megner, L.: Exploring noctilucent cloud variability using the nudged and extended version of the Canadian Middle Atmosphere Model, J. Atmos. Solar-Terr. Phys., 164, 276-288, doi:10.1016/j.jastp.2017.08.019, 2017.

Lambert, A., Read, W. G., Livesey, N. J., Santee, M. L., Manney, G. L., Froidevaux, L., Wu, D. L., Schwartz, M. J., Pumphrey, H. C., Jimenez, C., Nedoluha, G. E., Cofield, R. E.,

Cuddy, D. T., Daffer, W. H., Drouin, B. J., Fuller, R. A., Jamot, R. F., Knosp, B. W., Pickett, H. M., Perun, V. S., Snyder, W. V., Stek, P. C., Thurstans, R. P., Wagner, P. A., Waters, J. W., Jucks, K. W., Toon, G. C., Stachnik, R. A., Bernath, P. A., Boone, C. D., Walker, K. A., Urban, J., Murtagh, D., Elkins, J. W., and Atlas, E.: Validation of the Aura Microwave Limb Sounder middle atmosphere water vapor and nitrous oxide measurements, J. Geophys. Res., 112, D24S36, doi:10.1029/2007JD008724, 2007.

Lumpe, J., Bailey, S., Carstens, J., Randall, C., Rusch, D., Thomas, G., Nielsen, K., Jeppesen, C., McClintock, W., Merkel, A., Riesberg, L., Templeman, B., Baumgarten, G., and Russell III, J. M.: Retrieval of polar mesospheric cloud properties from CIPS: Algorithm description, error analysis and cloud detection sensitivity, J. Atmos. Solar-Terr. Phys., 104, 167-196, doi:10.1016/j.jastp.2013.06.007, 2013.

Pertsev, N., Dalin, P., Perminov, V., Romejko, V., Dubretis, A., Balčiunas, R., Čarnes, K., and Zalcik, M.: Noctilucent clouds observed from the ground: sensitivity to mesospheric parameters and long-term time series, Earth, Planets and Space, 66, 98, doi:earth-planets-space.com/content/66/1/98, 2014.

Peters, D. H. W., Entzian, G., and Keckhut, P.: Mesospheric temperature trends derived from standard phase-height measurements, J. Atmos. Solar Terr. Phys., 163, 23-30, doi:10.1016/j.jastp.2017.04.007, 2017.

Remsberg, E. E., Marshall, B. T., Garcia-Comas, M., Krueger, D., Lingenfelser, D. L., Martin-Torres, J., Mlynczak, M. G., Russell III, J. M., Smith, A. K., Zhao, Y., Brown, C., Gordley, L. L., Lopez-Gonzales, M. J., Lopez-Puertas, M., She, C.-Y., Taylor, M. J., and Thompson, R. E.: Assessment of the quality of the Version 1.07 temperature-versus-pressure profiles of the middle atmosphere from TIMED/SABER, J. Geophys. Res., 113, D17101, doi:10.1029/2008JD010013, 2008.

Rong, P. P., Russell III, J. M., Randall, C. E., Bailey, S. M., and Lambert, A.: Northern PMC brightness zonal variability and its correlation with temperature and water vapor, J. Geophys. Res. Atmos., 119, 2390-2408, doi:10.1002/2013JD020513, 2014.

Schmidt, F., Baumgarten, G., Berger, U., Fiedler, J., and Lübken, F.-J.: Local time dependence of polar mesospheric clouds: a model study, Atmos. Chem. Phys., 18, 8893-8908, doi:10.5194/acp-18-8893-2018, 2018.

Schwartz, M. J., Lambert, A., Manney, G. L., Read, W. G., Livesey, N. J., Froidevaux, L., Ao, C. O., Bernath, P. A., Boone, C. D., Cofield, R. E., Daffer, W. H., Drouin, B. J., Fetzer, E. J., Fuller, R. A., Jamot, R. F., Jiang, J. H., Jiang, Y. B., Knosp, B. W., Krüger, K., Li, J.-L. F., Mlynczak, M. G., Pawson, S., Russell III, J. M., Santee, M. L., Snyder, W. V., Stek, P. C., Thurstans, R. P., Tompkins, A. M., Wagner, P. A., Walker, K. A., Waters, J. W., and Wu, D. L.: Validation of the Aura Microwave Limb Sounder temperature and geopotential height measurements, J. Geophys. Res., 113, D15S11, doi:10.1029/2007JD008783, 2008.

601 Seftor, C. J., Jaross, G., Kowitt, M., Haken, M., Li, J., and Flynn, L. E.: Postlaunch performance
602   of the Suomi National Polar-orbiting Partnership Ozone Mapping and Profiler Suite
603   (OMPS) nadir sensors, J. Geophys. Res. Atmos., 119, doi:10.1002/2013JD020472, 2014.
604
605 Shettle, E. P., DeLand, M. T., Thomas, G. E., and Olivero, J. J.: Long term variations in the
606   frequency of polar mesospheric clouds in the Northern Hemisphere from SBUV,
607   Geophys. Res. Lett., 36, L02803, doi:10.1029/2008GL036048, 2009.
608
609 Siskind, D. E., Stevens, M. H., and Englert, C. E.: A model study of global variability in
610   mesospheric   cloudiness,   J.   Atmos.   Solar   Terr.   Phys.,   67,   501-513,
611   doi:10.1016/j.jastp.2004.11.007, 2005.
612
613 Siskind, D. E., Stevens, M. H., Hervig, M. E., and Randall, C. E.: Recent observations of high
614   mass density polar mesospheric clouds: A link to space traffic?, Geophys. Res. Lett., 40,
615   2813-2817, doi:10.1002/grl.50540, 2013.
616
617 Stevens, M. H., Lieberman, R. S., Siskind, D. E., McCormack, J. P. Hervig, M. E., and Englert,
618   C. E.: Periodicities of polar mesospheric clouds inferred from a meteorological analysis
619   and forecast system, J. Geophys. Res. Atmos., 122, 4508-4527,
620   doi:10.1002/2016JD025349, 2017.
621
622 Thomas, G. E., McPeters, R. D., and Jensen, E. J.: Satellite observations of polar mesospheric
623   clouds by the Solar Backscattered Ultraviolet radiometer: Evidence of a solar cycle
624   dependence, J. Geophys. Res., 96, 927-939, 1991.
625
626 Thomas, G. E., Lumpe, J., Bardeen, C., and Randall, C. E.: Albedo-Ice regression method for
627   determining ice water content of Polar Mesospheric Clouds using ultraviolet observations
628   from space, Atmos. Meas. Tech. Discuss., doi:10.5194/amt-2018-330, 2018.
629
630 von Savigny, C., DeLand, M. T., and Schwartz, M. J.: First identification of lunar tides in
631   satellite observations of noctilucent clouds, J. Atmos. Solar-Terr. Phys., 162, 116-121,
632   doi:10.1016/j.jastp.2016.07.002, 2017.
633
634 Weatherhead, E. C., Reinsel, G. C., Tiao, G. C., Meng, X.-L., Choi, D., Cheang, W.-K., Keller,
635   T., DeLuisi, J., Wuebbles, D. J., Kerr, J. B., Miller, A. J., Oltmans, S. J., and Frederick, J.
636   E.: Factors affecting the detection of trends: Statistical considerations and applications
637   to environmental data, J. Geophys. Res., 103, 17,149-17,161, 1998.
638
639

Table 1(a)

Statistics for NOAA-19 SBUV/2 Northern Hemisphere PMC Seasons, 2009-2018

Latitude	Season	Ntotal	Ncloud	LTasc	LTdesc	SCAasc	SCAdesc
50°-64° N	2009	8964	190	12.9	3.0	142.7°	93.5°
	2010	8624	67	12.7	2.9	143.4°	93.1°
	2011	8525	90	12.6	2.8	143.7°	92.9°
	2012	8366	95	12.6	2.8	143.7°	92.9°
	2013	8661	119	12.7	2.8	143.4°	93.1°
	2014	8912	153	12.9	3.1	142.8°	93.5°
	2015	9683	78	13.3	3.4	141.6°	94.2°
	2016	11019	228	13.7	3.8	139.4°	95.2°
	2017	13639	309	14.4	4.4	135.7°	96.6°
	2018	16364	246	15.1	5.1	130.5°	100.1°
64°-74° N	2009	11764	873	12.3	3.5	132.0°	98.5°
	2010	11654	645	12.0	3.3	132.2°	98.0°
	2011	11582	858	11.9	3.2	132.2°	97.7°
	2012	11380	694	11.9	3.2	132.2°	97.7°
	2013	11647	1094	12.0	3.3	132.1°	98.0°
	2014	11850	927	12.2	3.6	132.1°	98.6°
	2015	12273	882	12.6	3.9	131.8°	99.8°
	2016	12543	836	13.0	4.4	131.2°	101.4°
	2017	12567	662	13.6	5.0	129.6°	104.2°
	2018	12758	1124	14.4	5.8	127.2°	108.2°
74°-82° N	2009	15264	3286	9.9	5.3	120.5°	108.2°
	2010	15349	2525	9.7	5.1	120.2°	107.6°
	2011	15276	2803	9.6	5.0	120.1°	107.4°
	2012	15008	2345	9.6	5.0	120.1°	107.4°
	2013	15223	3428	9.7	5.1	120.1°	107.6°
	2014	15134	2769	9.9	5.4	120.5°	108.3°
	2015	15144	3216	10.3	5.8	121.2°	109.6°
	2016	15084	2740	10.8	6.3	121.7°	111.1°
	2017	14944	2339	11.4	7.0	121.9°	112.8°
	2018	15066	3150	12.2	7.7	121.9°	115.1°

Ntotal = Number of samples in latitude band during season (DSS = [-20,+55])

Ncloud = Number of PMC detections

LTasc = Average local time for ascending node samples [hr]

LTdesc = Average local time for descending node samples [hr]

SCAasc = Average scattering angle for ascending node samples

SCAdesc = Average scattering angle for ascending node samples

Table 1(b)

Statistics for NOAA-19 SBUV/2 Southern Hemisphere PMC Seasons, 2009-2018

Latitude	Season	Ntotal	Ncloud	LTasc	LTdesc	SCAasc	SCAdesc
50°-64° S	2009-2010	8355	45	14.7	–	133.3°	–
	2010-2011	8321	19	14.5	–	134.4°	–
	2011-2012	8134	7	14.5	–	134.7°	–
	2012-2013	8270	52	14.5	–	143.7°	–
	2013-2014	8259	14	14.7	–	143.4°	–
	2014-2015	8363	15	15.0	–	142.8°	–
	2015-2016	8353	11	15.4	–	141.6°	–
	2016-2017	8268	44	16.0	–	139.4°	–
	2017-2018	8336	33	16.7	–	135.7°	–
64°-74° S	2009-2010	8479	499	15.4	16.6	122.8°	93.9°
	2010-2011	8468	37	15.2	22.9	123.5°	94.0°
	2011-2012	8302	69	15.2	23.6	123.7°	94.0°
	2012-2013	8433	471	15.2	23.5	123.5°	94.0°
	2013-2014	8383	161	15.4	18.8	122.6°	93.9°
	2014-2015	8542	130	15.7	7.9	121.3°	93.9°
	2015-2016	8709	121	16.1	0.5	119.3°	93.9°
	2016-2017	9051	472	16.7	1.1	116.5°	94.1°
	2017-2018	10246	363	17.4	1.9	112.8°	94.5°
74°-82° S	2009-2010	15144	2495	17.2	21.7	112.8°	101.4°
	2010-2011	15052	481	17.0	21.6	113.3°	101.6°
	2011-2012	14664	672	17.0	21.5	113.5°	101.7°
	2012-2013	14905	2440	17.1	21.5	113.3°	101.6°
	2013-2014	14777	1409	17.2	21.7	112.7°	101.3°
	2014-2015	14934	753	17.6	22.1	111.7°	100.8°
	2015-2016	14876	741	18.0	20.5	110.4°	100.4°
	2016-2017	14636	2328	18.6	16.5	108.8°	110.1°
	2017-2018	14732	1883	19.3	12.4	106.7°	99.8°

Ntotal = Number of samples in latitude band during season (DSS = [-20,+55])

Ncloud = Number of PMC detections

LTasc = Average local time for ascending node samples [hr]

LTdesc = Average local time for descending node samples [hr]. Note that some latitude bands can combine times close to 24 hr and close to 0 hr

SCAasc = Average scattering angle for ascending node samples

SCAdesc = Average scattering angle for ascending node samples

Table 1(c)

Statistics for S-NPP OMPS NP Northern Hemisphere PMC Seasons, 2012-2018

Latitude	Season	Ntotal	Ncloud	LTasc	LTdesc	SCAasc	SCAdesc
50°-64° N	2012	5148	126	12.5	2.6	143.6°	92.6°
	2013	6378	119	12.5	2.6	143.5°	92.6°
	2014	6532	160	12.6	2.7	143.4°	92.6°
	2015	6415	86	12.6	2.7	143.5°	92.6°
	2016	6900	124	12.5	2.6	143.4°	92.6°
	2017	7215	161	12.5	2.6	143.4°	92.6°
	2018	7238	186	12.5	2.6	143.5°	92.7°
64°-74° N	2012	6472	385	11.8	3.0	131.7°	96.7°
	2013	8658	796	11.8	3.1	131.8°	96.9°
	2014	8598	722	11.9	3.2	131.8°	97.2°
	2015	8476	709	11.9	3.2	131.8°	97.1°
	2016	9320	201	11.8	3.1	131.8°	96.9°
	2017	9792	457	11.8	3.1	131.8°	96.9°
	2018	9837	884	11.8	3.1	131.8°	96.9°
74°-82° N	2012	8695	1497	9.5	4.9	119.5°	106.4°
	2013	11552	2935	9.5	4.9	119.6°	106.7°
	2014	11244	2272	9.6	5.0	119.7°	107.1°
	2015	11142	2591	9.6	4.9	119.7°	106.8°
	2016	12363	1894	9.5	4.9	119.6°	106.6°
	2017	12985	2008	9.5	4.9	119.6°	106.6°
	2018	13024	3139	9.5	4.9	119.6°	106.7°

Ntotal = Number of samples in latitude band during season (DSS = [-20,+55])

Ncloud = Number of PMC detections

LTasc = Average local time for ascending node samples [hr]

LTdesc = Average local time for descending node samples [hr]

SCAasc = Average scattering angle for ascending node samples

SCAdesc = Average scattering angle for ascending node samples

Table 1(d)

Statistics for S-NPP OMPS NP Southern Hemisphere PMC Seasons, 2012-2018

Latitude	Season	Ntotal	Ncloud	LTasc	LTdesc	SCAasc	SCAdesc
50°-64° S	2012-2013	5624	37	14.3	–	136.3°	–
	2013-2014	6217	15	14.4	–	135.5°	–
	2014-2015	6009	23	14.5	–	135.2°	–
	2015-2016	5929	11	14.4	–	135.7°	–
	2016-2017	7056	28	14.3	–	135.9°	–
	2017-2018	7140	45	14.3	–	135.9°	–
64°-74° S	2012-2013	5652	333	15.0	23.5	124.9°	94.6°
	2013-2014	6342	135	15.1	23.6	124.4°	94.6°
	2014-2015	6115	104	15.1	23.7	124.2°	94.5°
	2015-2016	6024	53	15.1	23.6	124.5°	94.6°
	2016-2017	7187	251	15.0	23.6	124.7°	94.6°
	2017-2018	7278	343	15.0	23.6	124.6°	94.6°
74°-82° S	2012-2013	9819	1781	16.9	21.5	114.3°	102.3°
	2013-2014	11076	1022	17.0	21.5	113.9°	102.0°
	2014-2015	10821	538	17.0	21.6	113.8°	102.0°
	2015-2016	10631	326	16.9	21.5	114.0°	102.1°
	2016-2017	12593	1619	16.9	21.5	114.2°	102.2°
	2017-2018	12756	1522	16.9	21.5	114.1°	102.2°

Ntotal   = Number of samples in latitude band during season (DSS = [-20,+55])

Ncloud   = Number of PMC detections

LTasc   = Average local time for ascending node samples [hr]

LTdesc   = Average local time for descending node samples [hr]

SCAasc   = Average scattering angle for ascending node samples

SCAdesc   = Average scattering angle for ascending node samples

Table 2(a)

Regression Fit Results for IWC, Northern Hemisphere, 1979-1997

Latitude	A(±dA)	R_{time}	B(±dB)	R_{solar}	C	Lag	Trend	Conf	Cycle
50-64 N	0.28(±0.14)	0.50	-1.27(±0.87)	-0.44	62.1	0.5	**4.8**	2.3	-5.5
64-74 N	0.47(±0.22)	0.57	-6.41(±1.53)	-0.77	104.6	1.0	**6.0**	3.3	**-20.5**
74-82 N	0.65(±0.22)	0.70	-6.52(±1.38)	-0.82	115.2	0.5	**7.2**	2.8	**-18.3**
50-82 N	0.62(±0.21)	0.70	-5.89(±1.32)	-0.81	108.3	0.5	**7.1**	2.7	**-17.3**

Table 2(b)

Regression Fit Results for IWC, Northern Hemisphere, 1998-2018

Latitude	A(±dA)	R_{time}	B(±dB)	R_{solar}	C	Lag	Trend	Conf	Cycle
50-64 N	0.20(±0.11)	0.59	-1.05(±1.09)	-0.45	57.9	0.5	**3.4**	0.9	-4.5
64-74 N	0.42(±0.18)	0.57	-0.82(±2.02)	-0.27	73.5	1.0	**5.1**	1.6	-2.5
74-82 N	0.24(±0.18)	0.44	-2.21(±1.75)	-0.43	98.1	0.5	**2.6**	1.5	-5.8
50-82 N	0.30(±0.17)	0.49	-1.48(±1.66)	-0.36	88.8	0.5	**3.3**	1.5	-4.1

Table 3(a)

Regression Fit Results for IWC, Southern Hemisphere, 1979-1997

Latitude	A(±dA)	R_{time}	B(±dB)	R_{solar}	C	Lag	Trend	Conf	Cycle
50-64 S	0.98(±0.26)	0.54	+4.87(±1.92)	+0.19	24.9	0.5	**17.3**	5.1	**+21.8**
64-74 S	0.51(±0.23)	0.59	-1.06(±1.54)	-0.41	70.3	0.0	**7.3**	4.6	-3.8
74-82 S	0.45(±0.25)	0.57	-1.38(±1.65)	-0.44	85.3	0.0	**5.4**	4.5	-4.2
50-82 S	0.53(±0.24)	0.61	-0.94(±1.60)	-0.41	79.9	0.0	**6.6**	4.4	-3.0

Table 3(b)

Regression Fit Results for IWC, Southern Hemisphere, 1998-2018

699

Latitude	A(±dA)	R_{time}	B(±dB)	R_{solar}	C	Lag	Trend	Conf	Cycle
50-64 S	-0.08(±0.27)	0.07	-2.97(±2.83)	-0.32	69.7	0.5	-1.4	2.5	-13.8
64-74 S	0.15(±0.23)	0.32	-3.38(±2.05)	-0.44	81.9	0.0	2.1	2.4	-12.0
74-82 S	0.14(±0.24)	0.31	-4.22(±2.18)	-0.46	97.4	0.0	1.7	2.6	-12.9
50-82 S	0.14(±0.23)	0.31	-3.92(±2.12)	-0.46	92.2	0.0	1.7	2.6	-12.2

700

701

702

703   Multiple regression fit parameters for SBUV merged seasonal average IWC data, using the form

704

705   $$IWC = A*(t_{center} - 1979.0) + B*F_{Ly\alpha}(t_{center} - t_{lag}) + C$$

706

707   t_{center} = mid-point of PMC season (DSS = [-20,+55]) [years]

708   $F_{Ly\alpha}$ = Lyman alpha flux averaged over PMC season, scaled by 1×10^{11} photons cm^{-2} sec^{-1} nm^{-1}

709   R_{time} = correlation coefficient of secular term

710   R_{solar} = correlation coefficient of solar term

711   t_{lag} = phase lag of solar term for fit with smallest χ^2 value [years]

712   Trend   = decadal change in IWC [%]. **Bold** values exceed 95% confidence level.

713   Conf   = amount of decadal change required to exceed 95% confidence level [%]

714   Cycle   = calculated variation in IWC from solar minimum to solar maximum [%], using a

715   Lyman alpha flux range of 2.6×10^{11} photons cm^{-2} sec^{-1} nm^{-1}. **Bold** values exceed 95%

716   significance of regression fit coefficient.

717